

# Ni(OH)<sub>2</sub> microspheres in situ self-grown on ultra-thin layered g-C<sub>3</sub>N<sub>4</sub> as a heterojunction electrocatalyst for oxygen evolution reaction

Tong Li<sup>a</sup>, Xinxia Ma<sup>a</sup>, Jiang Wu<sup>a,\*</sup>, Fenghong Chu<sup>b</sup>, Lingxia Qiao<sup>a</sup>, Yubao Song<sup>c</sup>,  
Maoliang Wu<sup>a</sup>, Jia Lin<sup>d</sup>, Lin Peng<sup>d</sup>, Zhongwei Chen<sup>e,\*</sup>

<sup>a</sup> College of Energy and Mechanical Engineering, Shanghai University of Electric Power, No. 2103 Pingliang Road, Shanghai 200090, China

<sup>b</sup> College of Electronics and Information Engineering, Shanghai University of Electric Power, Shanghai 200090, China

<sup>c</sup> Xi'an Thermal Power Research Institute Co., Ltd, Suzhou Branch, Suzhou 215153, China

<sup>d</sup> College of Mathematics and Physics, Shanghai University of Electric Power, China

<sup>e</sup> Department of Chemical Engineering, Waterloo Institute for Nanotechnology, University of Waterloo, Waterloo, Ontario N2L3G1, Canada



## ARTICLE INFO

### Article history:

Received 9 September 2021

Revised 11 October 2021

Accepted 19 October 2021

Available online 27 October 2021

### Keywords:

Oxygen evolution reaction

Water splitting

Electrocatalyst

Ni(OH)<sub>2</sub>/g-C<sub>3</sub>N<sub>4</sub>

## ABSTRACT

Oxygen evolution reaction (OER), as a part reaction of the overall water splitting, is deemed as a prospective technology for large-scale energy storage. However, the sluggish kinetics (large overpotential) and the expensive cost of noble metal-based electrocatalysts (RuO<sub>2</sub> and IrO<sub>2</sub>) restrain the widespread usage of OER. Hence, the discovery of non-precious metal-based electrocatalysts with tiny overpotential, satisfactory current density and outstanding stability has become urgent. In this work, we have prepared ultra-thin layered g-C<sub>3</sub>N<sub>4</sub> by a two-step thermal peeling method and synthesized Ni(OH)<sub>2</sub>/g-C<sub>3</sub>N<sub>4</sub> composite by a simple one-step solvothermal method. Benefiting from the layered g-C<sub>3</sub>N<sub>4</sub> as substrate, the overpotential of Ni(OH)<sub>2</sub>/g-C<sub>3</sub>N<sub>4</sub> composite was just 240 mV at 10 mA cm<sup>-2</sup>, which gives an unexpected improvement in the electrochemical performance of the composite samples compared to pure Ni(OH)<sub>2</sub> ( $\eta = 460$  mV). Additionally, the formation of heterojunction effectively reduces the resistance to electron transport in OER, the resistance of Ni(OH)<sub>2</sub>/g-C<sub>3</sub>N<sub>4</sub> ( $R_{ct} = 38.8 \Omega$ ) is far smaller than those of bare Ni(OH)<sub>2</sub> ( $R_{ct} = 41.6 \Omega$ ) and layered g-C<sub>3</sub>N<sub>4</sub> ( $R_{ct} = 43.6 \Omega$ ) at the open circuit potential. Ni(OH)<sub>2</sub>/g-C<sub>3</sub>N<sub>4</sub> composite samples display outstanding electrochemical stability, maintaining 85% of initial current density for 12 h. Moreover, density functional theory (DFT) demonstrates that  $\Delta G_3$  of Ni(OH)<sub>2</sub>/g-C<sub>3</sub>N<sub>4</sub> composite ( $\eta = 0.46$  V) is much lower than that of bare Ni(OH)<sub>2</sub> ( $\eta = 0.64$  V). These undeniable results demonstrate that Ni(OH)<sub>2</sub>/g-C<sub>3</sub>N<sub>4</sub> composite materials is promising alternative materials to replace precious metal-based OER electrocatalysts in the field of water splitting.

© 2021 Elsevier Ltd. All rights reserved.

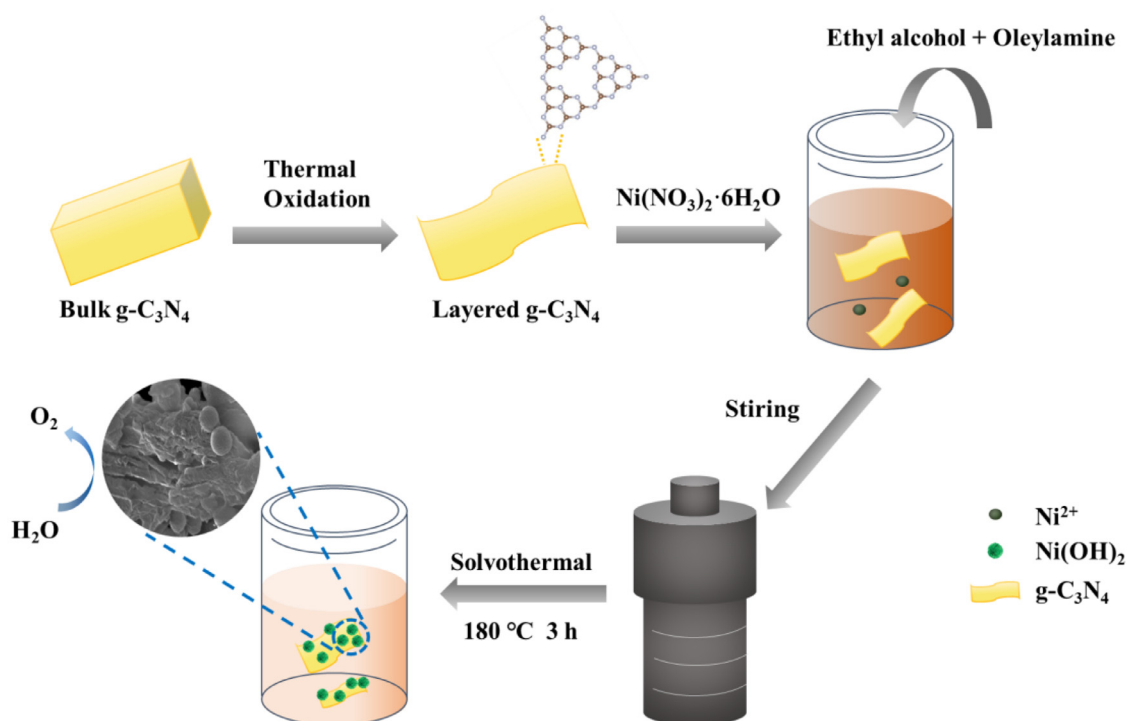
## 1. Introduction

Facing rapid global population growth and increasing demand for fossil fuels, attentions are increasingly being focused on sustainable and environmentally friendly power sources, thus the development of new energy is becoming urgent [1–3]. As an energy storage technology with high expectations, water splitting is considered to lead to an energy revolution because of its ability to obtain hydrogen from cheap, readily available and abundant water resources at a very low price [4–7]. Oxygen release at anode ( $4\text{OH}^- \rightarrow \text{O}_2 \uparrow + 2\text{H}_2\text{O} + 4\text{e}^-$ ) and hydrogen releases at cathode ( $4\text{H}_2\text{O} + 4\text{e}^- \rightarrow 2\text{H}_2 \uparrow + 4\text{OH}^-$ ). Both of them constitute overall water splitting ( $2\text{H}_2\text{O} \rightarrow 2\text{H}_2 \uparrow + \text{O}_2 \uparrow$ ) together [8,9]. However,

the sluggish kinetics and complex four protons multi-step transport process of the oxygen evolution reaction (OER) at anode is considered to be a stumbling block for high efficient overall water splitting, which usually demands overcoming an overpotential larger than ideal condition (1.23 V) to achieve the breakage of the H–O–H bond and the formation of the O=O bond, thus the oxygen evolution reaction greatly decreases the efficiency of overall water splitting [10–12]. Notably, precious metal oxides based catalysts (IrO<sub>2</sub> and RuO<sub>2</sub>) are usually considered as benchmark catalysts for OER and also serve as templates for the design of innovative catalysts [13–17]. However, the expensive cost of usage and disappointing stability restrict the massive use of IrO<sub>2</sub> and RuO<sub>2</sub> [18,19]. To solve this technical challenge, more effort needs to be devoted to the development of the earth's abundant non-precious metal elements based catalysts with tiny overpotential, impressive current density, extremely high catalytic activity, great durability, and low price [20,21].

\* Corresponding authors.

E-mail addresses: [wjcf2002@163.com](mailto:wjcf2002@163.com) (J. Wu), [zhwchen@uwaterloo.ca](mailto:zhwchen@uwaterloo.ca) (Z. Chen).



**Scheme 1.** Synthesis procedure of  $\text{Ni}(\text{OH})_2/\text{g-C}_3\text{N}_4$  composite catalyst.

Recently, single transition metal compounds have received much attentions, including single metallic hydroxides [22–24], phosphides [25], sulfides [26], nitrides [27], etc., which are considered as promising OER catalysts with potential to replace precious metal catalysts. Among these transition metal compounds, transition metal hydroxides have received additional discovery due to their excellent covalency, tiny bandgaps, and excellent water redox properties, all of which facilitate the acquisition of higher catalytic efficiency. As a widely studied metal hydroxide electrode material,  $\text{Ni}(\text{OH})_2$  is considered as an expected electrocatalyst for OER, due to its high catalytic performance and impressive stability. Gao and co-authors have prepared nanostructured  $\alpha\text{-Ni}(\text{OH})_2$  with overpotential of 331 mV at  $j = 10 \text{ mA cm}^{-2}$  [24]. Anantharaj and co-authors have reported the  $\text{Ni}(\text{OH})_2$  nanosheets with overpotential of 300 mV at  $j = 10 \text{ mA cm}^{-2}$  [28]. The above research illustrates that  $\text{Ni}(\text{OH})_2$  based OER catalysts have outstanding properties.

As is well known to all, choosing a suitable substrate can effectively improve the catalyst conductivity, provide more active sites, increase catalyst stability and catalytic performance [29,30]. Graphite carbon nitride ( $\text{g-C}_3\text{N}_4$ ) is a classic 2D  $\pi$ -conjugated layered material, which consists of two non-metallic elements, carbon and nitrogen [31]. Due to its simple fabrication, unique layered structure, low cost and chemical stability [32], it has been deeply researched in the field of photocatalytic water splitting [33]. Meanwhile, as a cheap substrate material that may replace graphene,  $\text{g-C}_3\text{N}_4$  has also received increasing attentions in the field of electrocatalytic water splitting.

In this work, we successfully synthesized highly efficient OER electrocatalysts by loading spherical  $\text{Ni}(\text{OH})_2$  on layered  $\text{g-C}_3\text{N}_4$  using a classic one-step solvothermal process for the first time. Pure spherical  $\text{Ni}(\text{OH})_2$  and layered  $\text{g-C}_3\text{N}_4$  exhibit disappointing catalytic properties. However, if the spherical  $\text{Ni}(\text{OH})_2$  grew on the layered  $\text{g-C}_3\text{N}_4$  by the solvothermal process, the composite samples exhibit unexpectedly excellent catalytic performance. The  $\text{Ni}(\text{OH})_2/\text{g-C}_3\text{N}_4$  composite samples possess an overpotential of only 240 mV at  $j = 10 \text{ mA cm}^{-2}$ , which is much smaller than those

of  $\text{Ni}(\text{OH})_2$  (470 mV) and  $\text{g-C}_3\text{N}_4$  (510 mV), and even smaller than that of  $\text{RuO}_2$  (360 mV). At the same time,  $\text{Ni}(\text{OH})_2/\text{g-C}_3\text{N}_4$  composite samples hold excellent stability and maintain high activity after a long test period of 12 h. These facts reveal the synergistic effect between spherical  $\text{Ni}(\text{OH})_2$  and layered  $\text{g-C}_3\text{N}_4$ . This impressive composite material is an expected alternative to  $\text{RuO}_2$  and  $\text{IrO}_2$  as an effective OER catalyst.

## 2. Experimental

### 2.1. Reagents and chemicals

$\text{Ni}(\text{NO}_3)_2 \cdot 6\text{H}_2\text{O}$ , Oleylamine, Melamine, Ethanol and Deionized water were purchased from Shanghai Titan Scientific CO., Ltd. All chemical reagents are analytical grade reagents and are used as received without further purification.

### 2.2. Synthesis

#### 2.2.1. Fabrication of layered $\text{g-C}_3\text{N}_4$ (LCN)

The LCN were prepared by the two-step thermal peeling process in advance. First, a ceramic crucible with lid containing 10 g of melamine was put in a muffle oven and heated to 550 °C for 2 h. The collected faint light-yellow bulk  $\text{g-C}_3\text{N}_4$  were milled in to powder. Then, 3 g of the light-yellow bulk  $\text{g-C}_3\text{N}_4$  powder was loaded into a ceramic crucible without lid and heated to 550 °C for another 1.5 h. The LCN was obtained after grounding.

#### 2.2.2. Fabrication of $\text{Ni}(\text{OH})_2/\text{g-C}_3\text{N}_4$ (NCN)

The NCN were prepared by the one-step solvothermal method displayed in Scheme 1. First, 1 mmol of  $\text{Ni}(\text{NO}_3)_2 \cdot 6\text{H}_2\text{O}$  were put into 20 mL ethyl alcohol, and vigorous magnetic stirring for 15 min. Then, 5.0 mg as-prepared LCN was dispersed in the mixed solution with another 15 min magnetic stirring. Finally, another 10 mL ethyl alcohol and 2 mL oleylamine were put into the mixed solution under magnetic stirring. The green solution was poured

into a 50 mL Teflon-lined autoclave and kept temperature at 180 °C for 3 h. The collected mixed solution was washed by deionized water and ethanol for four times at the room temperature, and then dried overnight at 80 °C. Obtained products were denoted as NCN, the synthesis process of bare  $\text{Ni}(\text{OH})_2$  was similar to the above without adding LCN.

### 2.2.3. Characterization

The powder X-ray powder diffraction with the range of  $2\theta = 5\text{--}80^\circ$  (XRD, rigaku Ultima IV, Cu  $K\alpha$  radiation,  $\lambda = 1.5418 \text{ \AA}$ ), X-ray photoelectron spectroscopy (XPS, Thermo Scientific K-Alpha) and energy dispersive X-ray (EDX) were used to probe the chemical composition of the matters. The scanning electron microscope (SEM, JSM-7800F), transmission electron microscopy (TEM, FEI G2 600–300), high resolution TEM (HRTEM TECNAI G2 TF20), and  $\text{N}_2$  adsorption/desorption isotherms (ASAP 2460 2.01,  $-195.8^\circ\text{C}$ ) were used to explore the structure of the samples. Fourier transform infrared spectra (FTIR, Thermo Scientific Nicolet iS5) was carried out to study the surface functional groups of catalysts with test range of  $4000\text{--}400 \text{ cm}^{-1}$ . Raman spectrum (Horiba:HR Evolution) was recorded in the test range of  $2000\text{--}400 \text{ cm}^{-1}$ .

### 2.3. Electrochemical measurements

CHI760E electrochemical workstation (CHI Instruments, CHN) was applied to conduct linear sweep voltammetry (LSV) curves, electrochemical impedance spectroscopy (EIS) and chronoamperometry. A standard three-electrode system was used, and a glassy carbon electrode ( $\sim 3 \text{ mm}$  in diameter), a  $\text{Hg}/\text{HgO}$  electrode with 1.0 M KOH filling solution and platinum plate ( $1 \text{ cm} \times 1 \text{ cm}$ ) was used as working electrode, reference electrode and counter electrode throughout the experiment, respectively. A 0.1 M KOH solution with  $\text{O}_2$ -saturated was used as electrolyte at room temperature. The potentials measured in our work were referenced to the reversible hydrogen electrode (RHE) through Nernst equation:

$$E(\text{RHE}) = E(\text{Hg}/\text{HgO}) + 0.098\text{V} + 0.059\text{pH} \quad (1)$$

To produce the ink, 2 mg of as-prepared  $\text{Ni}(\text{OH})_2/\text{g-C}_3\text{N}_4$  powder was dispersed into 1.0 mL mixed solution (750  $\mu\text{L}$  of deionized water, 250  $\mu\text{L}$  of isopropyl alcohol and 25  $\mu\text{L}$  of Nafion solution). Then, the mixture solution was ultrasonicated for at least 0.5 h to form a homogeneous ink. Afterward, the uniform suspension ink was coated on the surface of the working electrode ( $\sim 0.2 \text{ mg cm}^{-2}$ ). Then, the as-prepared catalyst film was dried at room temperature.

### 2.4. Theoretical calculation

Density functional theory (DFT) calculations were performed by Materials Studio (MS) Dmol<sup>3</sup> code. The spin-polarized GGA BLYP functional was carried out to study the exchange and correlation effects. The convergence criterions for the maximum energy variation, the maximum atomic force and the maximum displacement are set as  $2.0 \times 10^{-5} \text{ Ha}$ , 0.004  $\text{Ha}/\text{\AA}$  and 0.004  $\text{\AA}$ , respectively. The threshold of self-consistent field (SCF) tolerance is set as  $1.0 \times 10^{-5} \text{ Ha}$  to be the convergence standard. In addition, the atomic basis set is specified as Double Numerical plus D-functions (DND), and the molecular orbital occupancy is performed by the smearing method with a value of 0.005 Ha.

## 3. Results and discussion

### 3.1. Crystal and phase analysis

The crystal phases of LCN, spherical  $\text{Ni}(\text{OH})_2$  and NCN were investigated by using XRD analysis. Fig. 1 displays that an intense

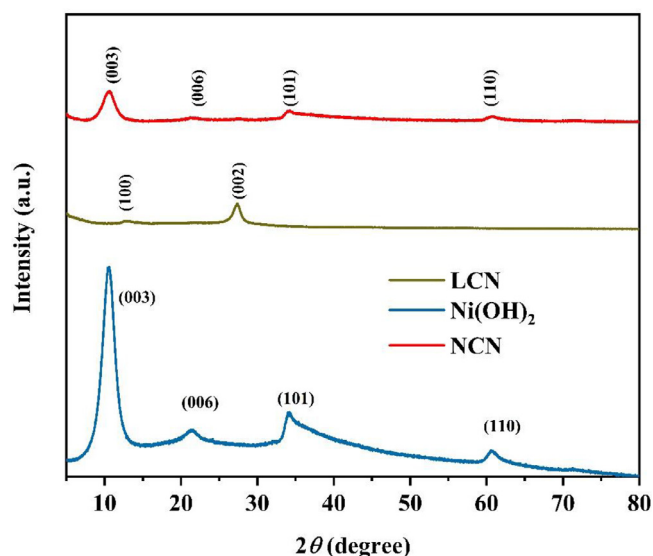


Fig. 1. XRD patterns of  $\text{Ni}(\text{OH})_2$ , LCN and NCN samples.

characteristic peak at  $2\theta = 27.41^\circ$  correspond to crystal plane of (002) of bare  $\text{g-C}_3\text{N}_4$ , which is coinciding with the characteristics of 2D stacked aromatic hydrocarbons. As the same time, an inconspicuous diffraction peak at  $2\theta = 12.6^\circ$  is ascribed to (001) lattice, due to a planar structural packing motif of tri-s-triazine units [34,35]. As for  $\text{Ni}(\text{OH})_2$ , the characteristic diffraction peaks at  $2\theta = 10.62^\circ$ ,  $21.12^\circ$ ,  $33.96^\circ$  and  $60.56^\circ$  are attributed to the (003), (006), (101) and (110) lattice planes, respectively, which correspond well with standard lattice of  $\text{Ni}(\text{OH})_2$  (JCPDS 380,715) [24]. NCN composite own diffraction peaks at the similar  $2\theta$  degrees with pure  $\text{Ni}(\text{OH})_2$ , demonstrating that the existence of LCN doesn't modify the crystal structure of  $\text{Ni}(\text{OH})_2$ . Notably, the amount of LCN in as-prepared sample may be too low to qualify for the assay [36]. To verify the presence of LCN in NCN composite samples and further investigate the surface morphology, SEM, EDX, TEM and HRTEM characterization are utilized in the following for demonstration.

### 3.2. Morphology and microstructure analysis

The surface nanomorphology and nanostructure of the as-prepared samples were carried out by SEM. As for bulk  $\text{g-C}_3\text{N}_4$  in Fig. 2a, indicating a large amount of layered  $\text{g-C}_3\text{N}_4$  is densely arranged into bulk  $\text{g-C}_3\text{N}_4$ . Moreover, as shown in Fig. 2b, after thermal peeling  $\text{g-C}_3\text{N}_4$  exists obvious layered structure composed of many ultra-thin 2D nanosheets, which theoretically has larger specific surface area and increases the active sites for better catalytic activity. From the SEM image of Fig. 2c, it could be clearly observed that the  $\text{Ni}(\text{OH})_2$  samples possess the morphology of microsphere, and the average diameter is approximately 1–1.2  $\mu\text{m}$ . As displayed in Fig. 2d,  $\text{Ni}(\text{OH})_2$  microspheres grow uniformly on LCN, leading to forming the heterostructure for NCN. What's more, the addition of LCN doesn't impact the microstructure of  $\text{Ni}(\text{OH})_2$ , demonstrating that  $\text{Ni}(\text{OH})_2$  microspheres and LCN have successfully coupled. EDX spectrum of NCN composite is revealed in Fig. 3b. It provides direct and valid evidence of the existence of elements such as C, N, O and Ni in the composite materials, revealing the successful synthesis of NCN composite by the solvothermal method. Fig. 3c–f. are the EDX elemental mapping images of NCN, which further demonstrates that C, N, O and Ni elements are evenly distributed in the composite materials, validating the successful synthesis of NCN.

In addition, TEM and HRTEM were applied to further explore the microstructure of as-prepared LCN,  $\text{Ni}(\text{OH})_2$  and NCN compos-



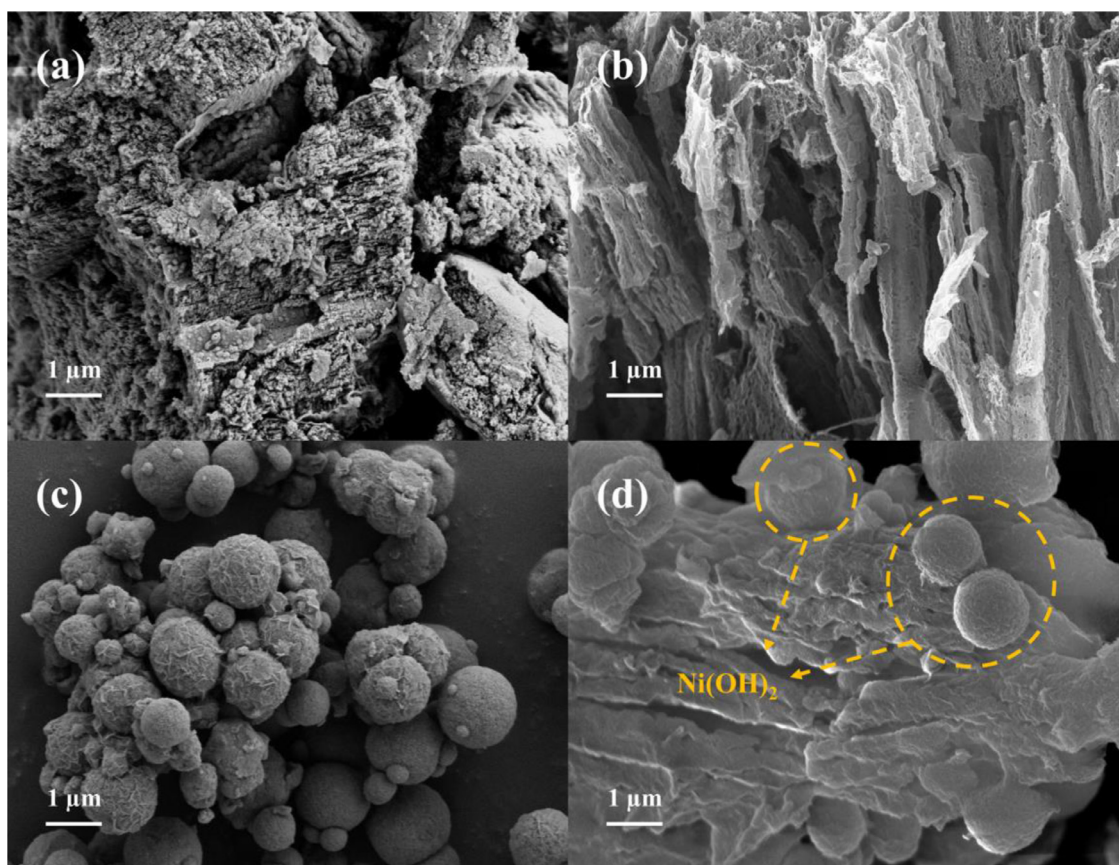


**Fig. 2.** SEM images of bulk g-C<sub>3</sub>N<sub>4</sub> (a), as-prepared LCN (b), Ni(OH)<sub>2</sub> (c), and NCN(d).

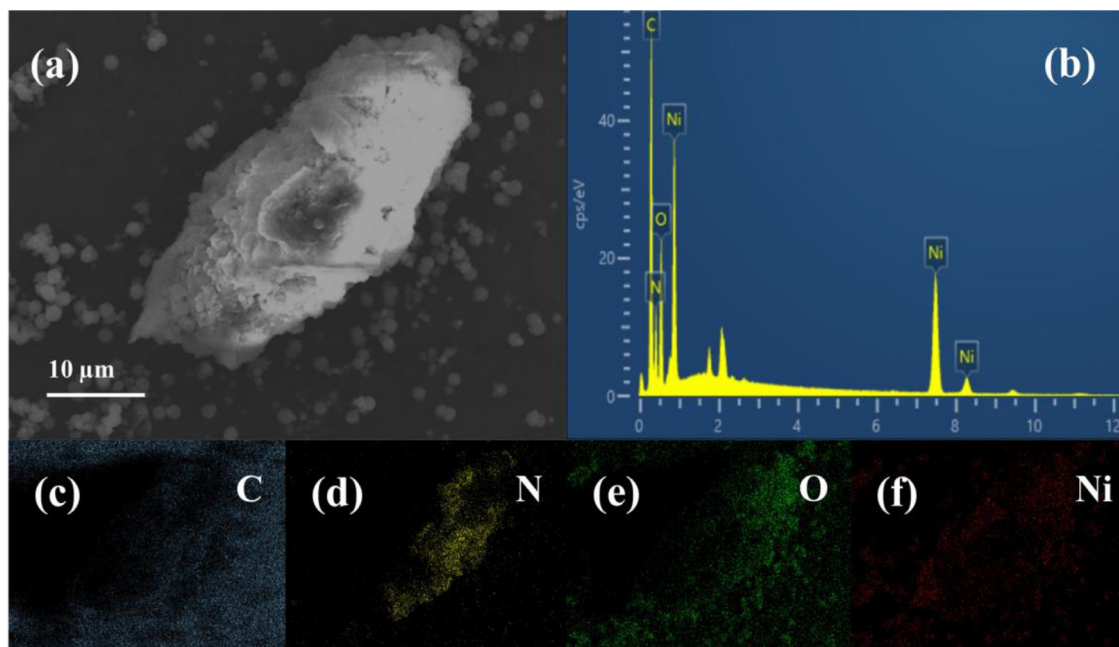


**Fig. 3.** The selected area of NCN composite (a); EDX spectrum (b) of NCN composite (b); EDX elemental mapping images of NCN composite: C (c), N (d), O (e) and Ni (f).

ite. As illustrated in Fig. 4a, pure LCN exhibits highly transparent ultrathin lamellar morphology. By the way, LCN is pliable and its edge portion is rolled, mainly due to preparing by high temperature thermal peeling. A good substrate provides the large enough specific surface area for supporting the catalyst, which is consistent with previous literature [37]. Fig. 4b indicates that the Ni(OH)<sub>2</sub> still

exhibits interdependent microsphere structures, in agreement with the results of SEM. Furthermore, it's clearly to observe Ni(OH)<sub>2</sub> microspheres on the LCN microsurface (Fig. 4c). One of them (orange circle) was enlarged, clearly, irregular LCN and highly parallel lattice fringes for Ni(OH)<sub>2</sub> in NCN composite were both found (Fig. 4d). The HRTEM image of NCN further confirmed the lat-

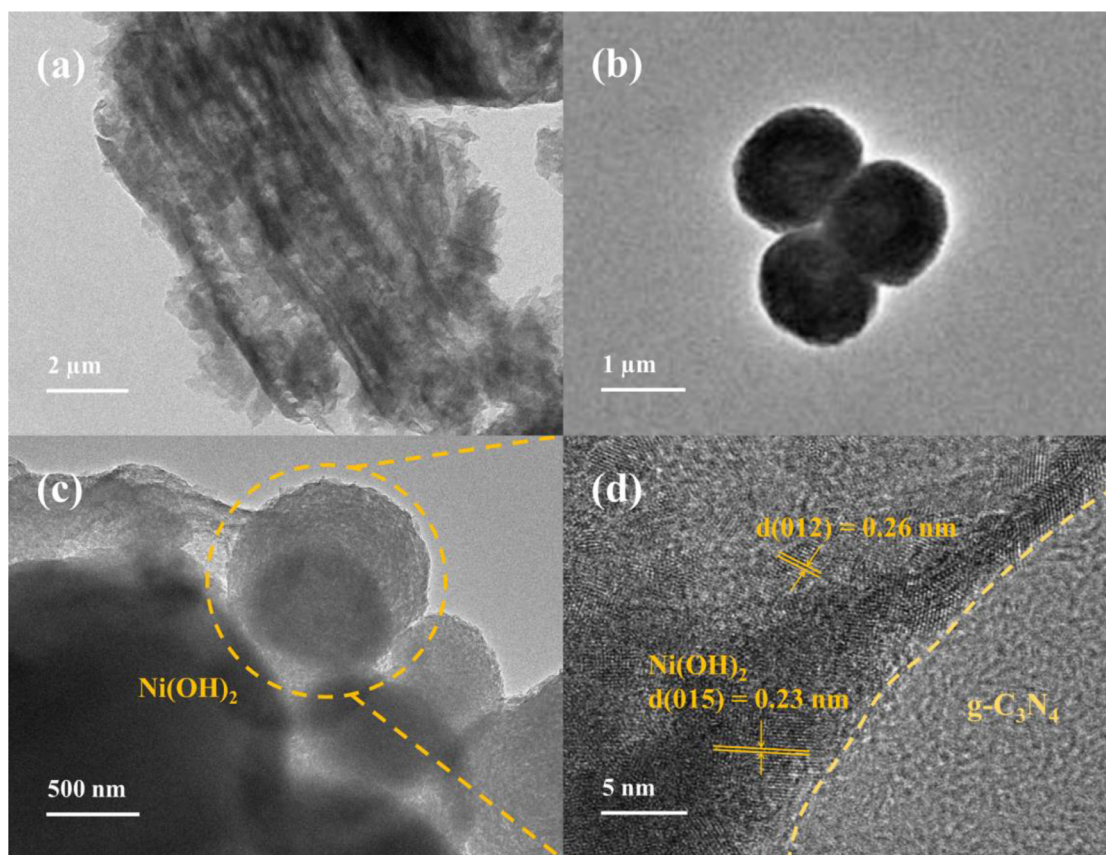


Fig. 4. TEM images of as-prepared LCN (a),  $\text{Ni(OH)}_2$  (b), and NCN(c); HRTEM image of NCN composite (d).

tice spacing of  $\text{Ni(OH)}_2$  are 0.23 and 0.26 nm, which could be indexed to the (015) and (012) atomic planes of  $\text{Ni(OH)}_2$ , respectively. What's more, the contact boundary between  $\text{Ni(OH)}_2$  and LCN could be clearly observed. This fact justifies that the NCN heterojunction was successfully formed via surface engineering.

To explore the effect of the addition of LCN on the specific surface area of composite samples, nitrogen adsorption-desorption isotherm was used. As displayed in Fig. 5a, all curves are type IV with H3 hysteresis loops, proving that all three samples own mesopores. Additionally, the pore size of LCN,  $\text{Ni(OH)}_2$  and NCN were calculated by the BJH (Barrett-Joyner-Halenda) method as 11.3, 9.6 and 9.5 nm, respectively, further proving the formation of mesopores. Simultaneously, the surface properties of three samples were calculated by the BET (Brunauer-Emmett-Teller) model as 14.1, 37.1 and 85.8  $\text{m}^2/\text{g}$  for LCN,  $\text{Ni(OH)}_2$  and NCN, respectively. Obviously, the specific surface area of NCN is larger than that of two bare samples. This result could be attributed to the fact that  $\text{Ni(OH)}_2$  microspheres assembled from numerous nanosheets were successfully compounded on LCN surface, thereby increasing the specific surface area of LCN. This evidence suggests that NCN has a better electrocatalytic potential. However, the chemistry of the catalyst is still unclear, therefore additional chemical characterization was used to investigate it further.

### 3.3. Chemical composition analysis

The Raman survey spectra of LCN is shown in Fig. 5b. Due to the oscillation of CN, the characteristic peaks could be clearly found at 477.8, 707.3, 753.6, and 982.6  $\text{cm}^{-1}$ , consisting of the deformation of the graphitic domains and the stretching mode of the s-triazine ring [38]. Additionally, the characteristic signals located at 1235.4 and 1482.6  $\text{cm}^{-1}$  were attributed to  $\text{C-N}$  and  $\text{C-N}$  vi-

brations, respectively [39]. These results directly prove the formation of graphitic nitrogen in  $\text{g-C}_3\text{N}_4$  via high temperature thermal peeling method.

To further investigate the surface functional groups and chemical composition of LCN,  $\text{Ni(OH)}_2$  and NCN, FTIR analysis was used in the range of 400–4000  $\text{cm}^{-1}$ . As shown in Fig. 5c, we can observe an absorption peak for LCN at 809  $\text{cm}^{-1}$ , which is corresponded to the breathing of s-triazine [40]. Moreover, other characteristic peaks are located at 1242, 1321, 1411, 1459, 1571 and 1636  $\text{cm}^{-1}$ , due to the tensile vibrations of CN heterocycles [40]. Generally, a broad band is associated with N–H stretching vibration in the range of 3100–3500  $\text{cm}^{-1}$ , due to the free  $\text{-NH}_2$  group in the matters [41]. The signal for Ni–OH metal bond is located at 527  $\text{cm}^{-1}$  [42], and the signal for unreacted  $\text{-OH}$  group in  $\text{Ni(OH)}_2$  is found at 3690  $\text{cm}^{-1}$  [43]. The pure  $\text{Ni(OH)}_2$  and NCN samples possess almost the same characteristic peaks, suggesting that the addition of LCN doesn't alter the chemical structure characteristics of bare  $\text{Ni(OH)}_2$  in the synthesis process.

The chemical state and covalent bonds of as-prepared electrocatalysts could be further proved via X-ray photoelectron spectroscopic (XPS) analysis. As displayed in Fig. 5d, clearly, the XPS survey spectra proves that C, N, O, and Ni elements are existed successfully in NCN, showing the perfect coupling of  $\text{Ni(OH)}_2$  and LCN. From the table S3, it's clearly to see the percent of C and N elements are only 6.07% and 1.23%, respectively, which agrees with the previous XRD analysis. In Fig. 5e–h, high-resolution XPS spectra of C 1s, N 1s, O 1s and Ni 2p for NCN represent corresponding characteristic peaks and binding energies, respectively. In Fig. 5e, the main signals of C 1s located at  $\sim 284.2$ ,  $\sim 284.9$ ,  $\sim 285.5$  and  $\sim 288.4$  eV correspond to the coordination of C–C, C–C, C–N and C–O bond, respectively [44]. It should be noted that the C–C bonds provide a direct evidence of the formation of the  $\text{sp}^2$  hy-



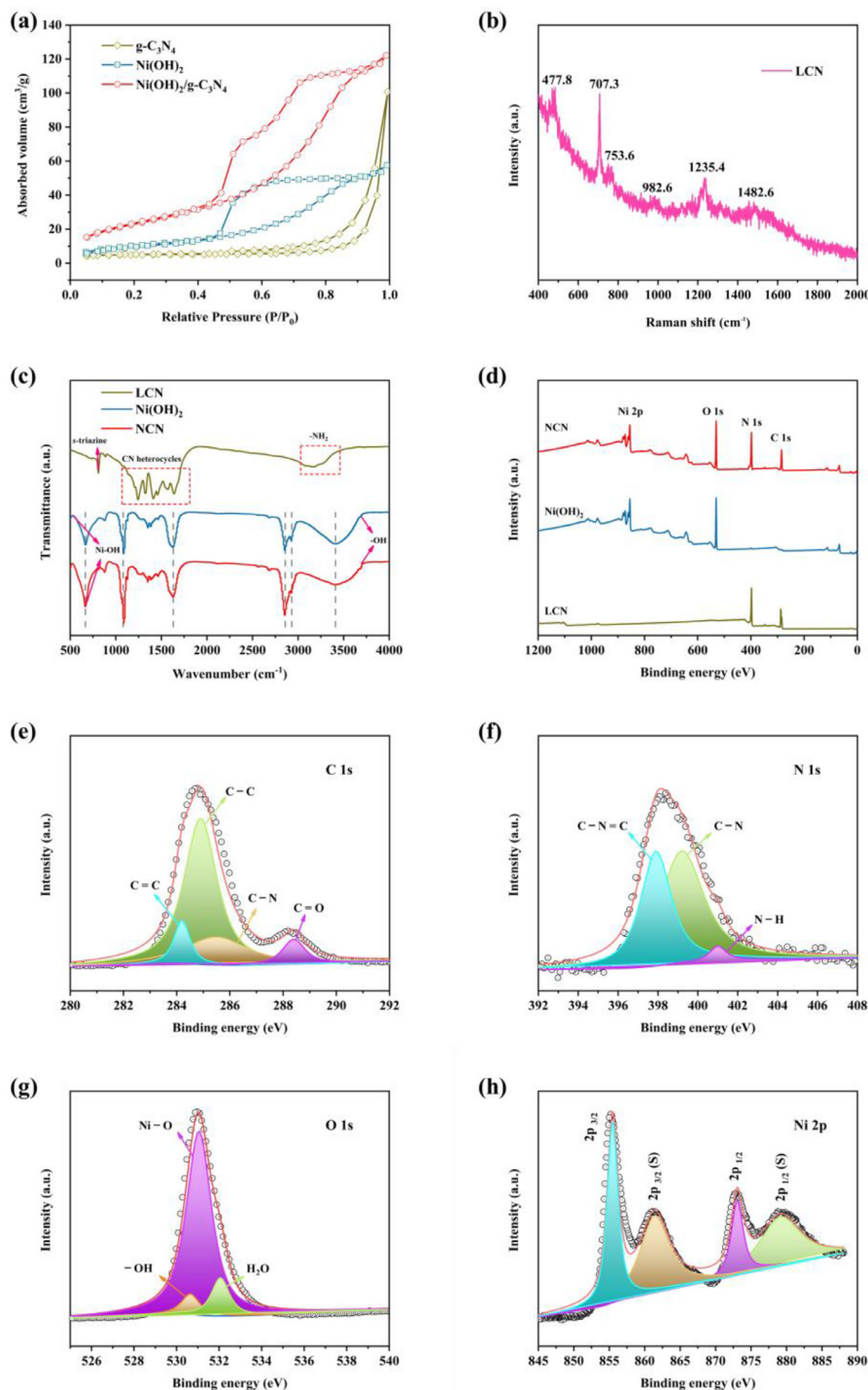


**Fig. 5.**  $N_2$  adsorption-desorption isotherms of  $g-C_3N_4$ ,  $Ni(OH)_2$  and  $Ni(OH)_2/g-C_3N_4$  catalysts (a); Raman spectra of LCN (b); FT-IR spectra of LCN,  $Ni(OH)_2$  and NCN catalysts (c); XPS spectra of LCN,  $Ni(OH)_2$  and NCN (d); High-resolution XPS spectra of C 1 s (e); N 1 s (f); O 1 s (g) and Ni 2p (h) for NCN.

bridized carbon. It can be seen that the N 1 s (Fig. 5f) could be fitted into three main Gaussian-Lorentzian signals. The signal centered at  $\sim 397.9$  eV belongs to the C–N=C (graphitic nitrogen). The signal located at  $\sim 399.2$  eV corresponds to C–N (pyridinic nitrogen). The signal existed at  $\sim 400.9$  eV related to N–H (amino function). In Fig. 5g, there are three distinctive singals located at  $\sim 530.6$ ,  $\sim 531.1$  and  $532.1$  eV in the O 1 s spectra, belonging to chemical adsorption of physical adsorption of water on or near the  $Ni(OH)_2$  surface, typical metal oxygen-bond and hydroxyls, respectively. Be-

sides, based on the deconvolution results of the high-resolution O 1 s region, the area of the metal oxygen-bond is much larger than those of the other two bonds, which seems to indicate that lattice oxygen plays an important role in the OER reaction. As for Ni 2p (Fig. 5h), two main characteristic signals at  $\sim 855.4$  and  $\sim 873.1$  eV belong to  $Ni\ 2p_{3/2}$  and  $Ni\ 2p_{1/2}$ , respectively. Meanwhile, two satellite signals at  $\sim 861.5$  and  $\sim 879.3$  eV also belong to  $Ni\ 2p_{3/2}$  and  $Ni\ 2p_{1/2}$ , respectively. Both of them prove that the  $Ni^{2+}$  ions remain stably in the composite materials. Hence, all above results have

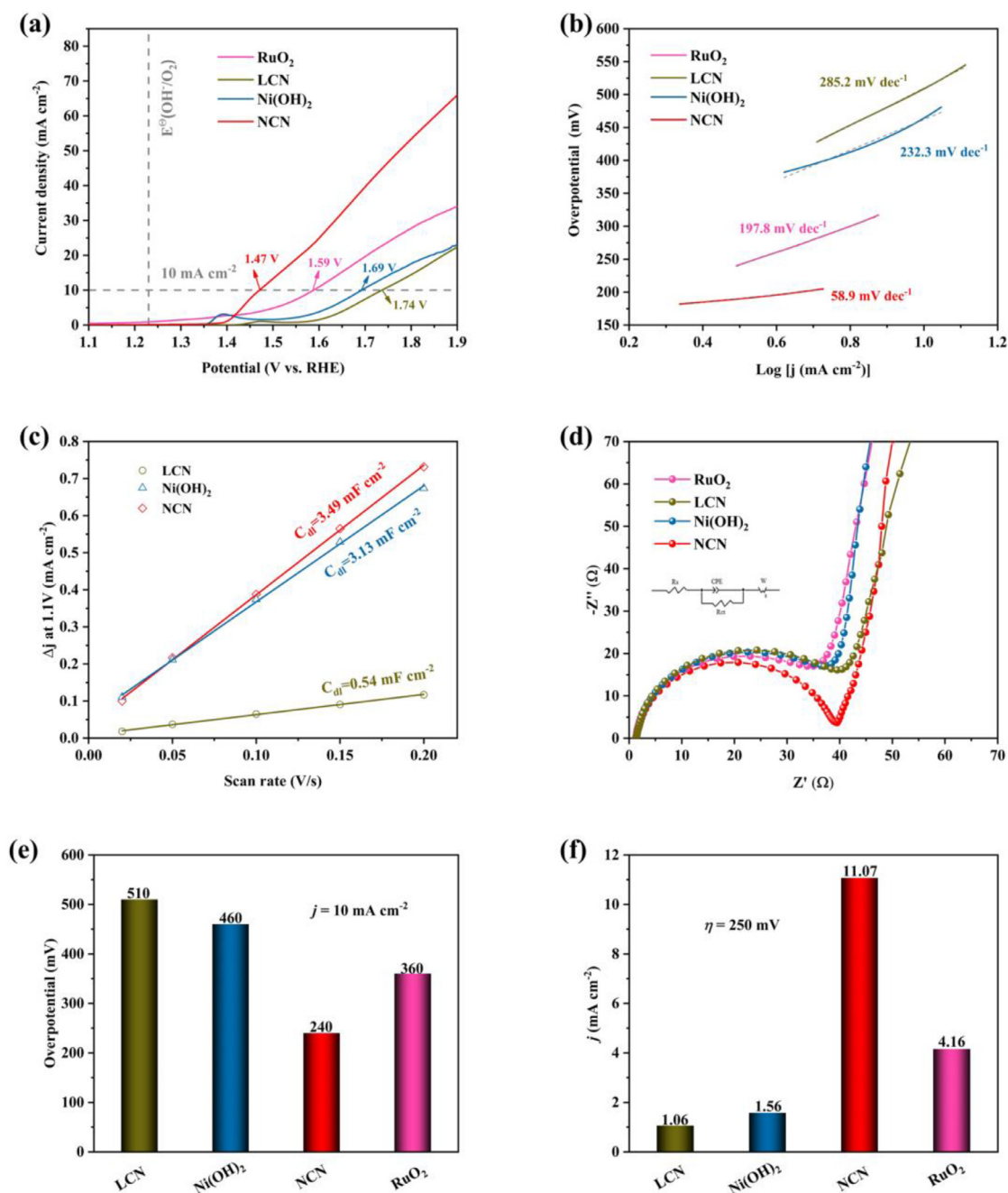


**Fig. 6.** Polarization curves (a) and Tafel plots (b) of LCN, Ni(OH)<sub>2</sub>, NCN and RuO<sub>2</sub>; the double-layer capacitance ( $C_{dl}$ ) measurements (c) (at 1.10 V vs. RHW) for LCN, Ni(OH)<sub>2</sub> and NCN; EIS (d), overpotential (e) at  $j = 10 \text{ mA cm}^{-2}$  and current density (f) at  $\eta = 250 \text{ mV}$  for LCN, Ni(OH)<sub>2</sub>, NCN and RuO<sub>2</sub>. All measurements were performed in O<sub>2</sub> purged 0.1 M KOH (pH  $\sim 13$ ). All LSV curves were recorded at a sweep rate of  $10 \text{ mV s}^{-1}$  with iR corrected.

proved the successful coupling of NCN binary composites in terms of chemical functional groups and chemical bonding demonstrated. However, the electrochemical properties of the catalyst remain unclear, so additional electrochemical measurements were applied.

### 3.4. Electrochemical measurements and properties

In general, electrocatalysts with low overpotential, high current density and low resistance values are considered to be a promising electrocatalyst for applications widely. We got electrochemical measurements of as-prepared samples in 0.1 M KOH solution at room temperature with  $\sim 0.2 \text{ mg cm}^{-2}$  ink density. Polarization curves recorded for the as-prepared samples are displayed in

Fig. 6a. Obviously, NCN composite reveals the highest OER catalytic activity, possessing the low overpotential of 240 mV at  $j = 10 \text{ mA cm}^{-2}$ , which is much lower than those of LCN (510 mV) and bare Ni(OH)<sub>2</sub> (460 mV), even RuO<sub>2</sub> ( $\eta = 360 \text{ mV}$ ) is also inferior than that of NCN (Fig. 6e). Pure Ni(OH)<sub>2</sub> has a clear oxidation peak near 1.4 V (vs. RHE), the phenomenon attributed to the oxidation of Ni<sup>2+</sup> to Ni<sup>3+</sup> [45,46]. Interestingly, the NCN composites don't exhibit significant oxidation peak based on the support of LCN, that can be ascribed to the coupling effect of the heterojunction successfully synthesized by Ni(OH)<sub>2</sub> and LCN. This result may proof the formation of heterojunction may improve the electrocatalytic performance of the catalysts. Furthermore, pure LCN, Ni(OH)<sub>2</sub> and RuO<sub>2</sub> only deliver current density of 1.06, 1.56 and

4.16 mA cm<sup>-2</sup> at  $\eta = 250$  mV, however, the current density of NCN composite could reach 11.07 mA cm<sup>-2</sup> at the same overpotential (Fig. 6f), indicating the loading of Ni(OH)<sub>2</sub> microsphere onto LCN to form heterojunction does enhance the electrocatalytic properties of the composite for OER. In a word, the construction of suitable heterostructure between Ni(OH)<sub>2</sub> and LCN could efficiently adjust the electronic properties. What's more, the robust LCN substrates in Ni(OH)<sub>2</sub>/LCN heterostructure could anchor the Ni(OH)<sub>2</sub> microspheres and prevent their aggregation, resulting in high exposure of the active sites, thereby facilitating the adsorption of OH<sup>-</sup>, reducing the electron transmission resistance and leading to a significantly enhanced electrocatalytic activity for OER. Tafel slope is a key parameter for OER to assess the intrinsic kinetic properties of the catalyst. Tafel slopes were carried out according to the Tafel formula:

$$\eta = a + b \cdot \log(j) \quad (2)$$

where  $\eta$  is overpotential,  $b$  is the Tafel slope,  $j$  is the current density and  $a$  is the Tafel constant. Notably, OER is a complex four protons multi-step reaction. Hence, the Tafel slopes only provide a reference for further studying the intrinsic kinetic characteristics of catalysts. Previous reports have generally assumed that a lower Tafel slope for electrocatalyst predicts that a higher current density can be achieved with a lower overpotential [46]. As displayed in Fig. 6b, NCN composite owns the lowest Tafel slope (58.9 mV dec<sup>-1</sup>). However, the Tafel slope of pure LCN, Ni(OH)<sub>2</sub> and RuO<sub>2</sub> are 285.2 mV dec<sup>-1</sup>, 232.3 mV dec<sup>-1</sup> and 197.8 mV dec<sup>-1</sup>, respectively. This fact demonstrates that NCN owns more efficient kinetics for OER than those of two pure samples and RuO<sub>2</sub>. The higher electrocatalytic activity can be attributed to that the addition of LCN effectively increases the rate of OH<sup>-</sup> adsorption and the charge transport.

Table S2 summarizes the OER performance of previously published work about nickel hydroxides based electrocatalysts. It's clearly to see that the materials synthesized in this report have lower overpotential compared to previous papers, indicating that as-prepared LCN composite has outstanding OER electrocatalytic performance.

Electrochemically active surface area (ECSA) is another key parameter for evaluating OER. Since ECSA is linearly proportional to  $C_{dl}$ , ECSA could be evaluated by calculating  $C_{dl}$ :

$$ECSA = \frac{C_{dl}}{C_s} \quad (3)$$

Where  $C_s$  is the specific capacitance of a smooth and planar electrode measured in the same experimental conditions. The value of 0.040 mF cm<sup>-2</sup> is used for  $C_s$ , which is based on a typical value for a metal electrode in the 0.1 M KOH solution [47]. The  $C_{dl}$  was obtained by sweeping cyclic voltammetry (CV) in 1.05–1.15 V vs.RHE by different scan rates from 20 to 200 mV s<sup>-1</sup>. In Fig. 6c, it's clearly to observe that the NCN composite exhibits the greater  $C_{dl}$  of 3.49 mF cm<sup>-2</sup> than those of bare LCN (0.54 mF cm<sup>-2</sup>) and Ni(OH)<sub>2</sub> (3.13 mF cm<sup>-2</sup>). ECSA has the similar trend with  $C_{dl}$ , the value of ECSA for NCN is 87 cm<sup>2</sup>, which is larger than those of LCN (13.5 cm<sup>2</sup>) and Ni(OH)<sub>2</sub> (78.3 cm<sup>2</sup>). Due to the broad surface and abundance of layers of LCN, NCN provides wider electrochemical reaction areas for the OER.

For further obtain additional OER kinetic characteristics of the electrocatalyst, we measured EIS at open circuit potential in the frequency range of 10<sup>6</sup>–10<sup>-1</sup> Hz. All fitted Nyquist plots, including for RuO<sub>2</sub>, LCN, Ni(OH)<sub>2</sub> and NCN, are displayed in Fig. 6d. Clearly, all curves exhibit the characteristics of standard Nyquist curve, i.e., a semicircle and a straight line exist in the high and low frequency range, respectively [48,49]. The radius of the semicircle in the high frequency range corresponds to the resistance ( $R_{ct}$ ) of the catalyst to transport electron in the OER, i.e., a smaller radius means a

lower resistance. The  $R_{ct}$  of RuO<sub>2</sub>, LCN, Ni(OH)<sub>2</sub> and NCN were calculated as 40.7, 43.6, 41.6 and 38.8  $\Omega$ , respectively, demonstrating the excellent charge transport properties and greater conductivity of NCN composite during the OER process.

In addition, the turnover frequency (TOF) was performed to support further understanding the intrinsic characteristics of electrocatalytic activity (Supporting Information), which is assumed that the Faraday efficiency was 100% and Ni atoms took the role of active sites for the OER. The TOF and other critical electrochemical parameters of as-prepared samples were listed in Table 1. Clearly, the TOF value of NCN was calculated as 0.188 s<sup>-1</sup> at the  $\eta = 350$  mV, which was much higher than those of LCN (0.009 s<sup>-1</sup>) and Ni(OH)<sub>2</sub> (0.025 s<sup>-1</sup>). Even the TOF value of RuO<sub>2</sub> (0.113 s<sup>-1</sup>), the benchmark catalyst, was also inferior to that of it. This result suggests that the coupling of NCN heterojunction, with the addition of LCN, resulting in facilitation of the catalysts' intrinsic properties, which favoured the OER kinetics.

What's more, exchange current density ( $J_0$ ) is also an important parameter for OER, which is influenced by electrode material, electrode surface state, electrolyte composition, and experimental temperature [50]. Exchange current density ( $J_0$ ) could be calculated as follows:

$$J_0 = \frac{RT}{nFR_{ct}} \quad (4)$$

Where  $R$  is the gas molar constant (8.314 J mol<sup>-1</sup> K<sup>-1</sup>),  $T$  is the experimental temperature (298 K at room temperature),  $n$  is the electron transfer number,  $F$  is the Faraday constant (96,485 C mol<sup>-1</sup>), and  $R_{ct}$  is the charge transfer resistance. It should be noted that the exchange current density of NCN is 0.17 mA cm<sup>-2</sup>, which is larger than those of LCN (0.14 mA cm<sup>-2</sup>), Ni(OH)<sub>2</sub> (0.15 mA cm<sup>-2</sup>), and RuO<sub>2</sub> (0.16 mA cm<sup>-2</sup>). Furthermore, exchange current density is proportional to the catalytic active area. The larger the  $J_0$ , The larger the specific surface area of the material, the faster the electron transfer rate and the better OER kinetics. Clearly, NCN owns larger specific surface area, faster electron transfer rate and superior OER kinetics.

Without excellent stability, electrocatalysts are difficult to popularize around the world. In this work, we took the polarization curves for NCN composite corresponding to the initial and after 5000 cycles. From the Fig. 7a, two curves were closed to each other and the overpotential for NCN at  $j = 10$  mA cm<sup>-2</sup> only increase 10 mV after 5000 CV cycles. This result indicates that the newly synthesized OER electrode material possesses good stability. What's more, we also carried out the chronoamperometry of as-prepared sample at 1.47 V (vs.RHE) to deliver  $j = 10$  mA cm<sup>-2</sup>. Surprisingly, after 12 h of extended testing, the current density remained at 8.5 mA cm<sup>-2</sup> (85% of the initial current) (Fig. 7b), while the microscopic morphology and nanostructure of the samples seem unchange significantly after the test (insert Fig. 7b).

To further probe the mechanisms of the outstanding OER performance of NCN, we use XPS analysis and HRTEM analysis to investigate the composition and microstructure changes after the long-term test. As shown in Fig. 7c, we can clearly observe the existence of NiOOH on the catalyst surface. XPS analysis is conducted to probe the surface electronic states after the long-term test. The change of O 1s state is essential to analyze the composition evolution of NCN. As shown in Fig. 7e, the area of the metal-oxygen bond peak significantly decreases after OER test, which is attributed to the release of the oxygen atoms in the metal-oxygen bonds during the electrocatalytic process. It can be seen from this fact that the high catalytic of the NCN does lie in the presence of lattice oxygen. Fig. 7f displays the Ni 2p spectrum after 12 h stability test. The broader Ni 2p<sub>3/2</sub> and Ni 2p<sub>1/2</sub> peaks can be deconvoluted into Ni<sup>2+</sup> and Ni<sup>3+</sup> [51,52]. The formation of Ni<sup>3+</sup> indi-



**Table 1**  
Summary of the electrochemical properties of the samples.

Samples	$\eta$ (mV)	Tafel slope (mV dec <sup>-1</sup> )	$R_{ct}$ ( $\Omega$ )	$J_0$ (mA cm <sup>-2</sup> )	$C_{dl}$ (mF cm <sup>-2</sup> )	ECSA (cm <sup>-2</sup> )	TOF (s <sup>-1</sup> )
LCN	510	285.2	43.6	0.14	0.54	13.5	0.009
Ni(OH) <sub>2</sub>	460	232.3	41.6	0.15	3.13	78.3	0.025
NCN	240	58.9	38.8	0.17	3.49	87	0.188
RuO <sub>2</sub>	360	197.8	40.7	0.16			0.113

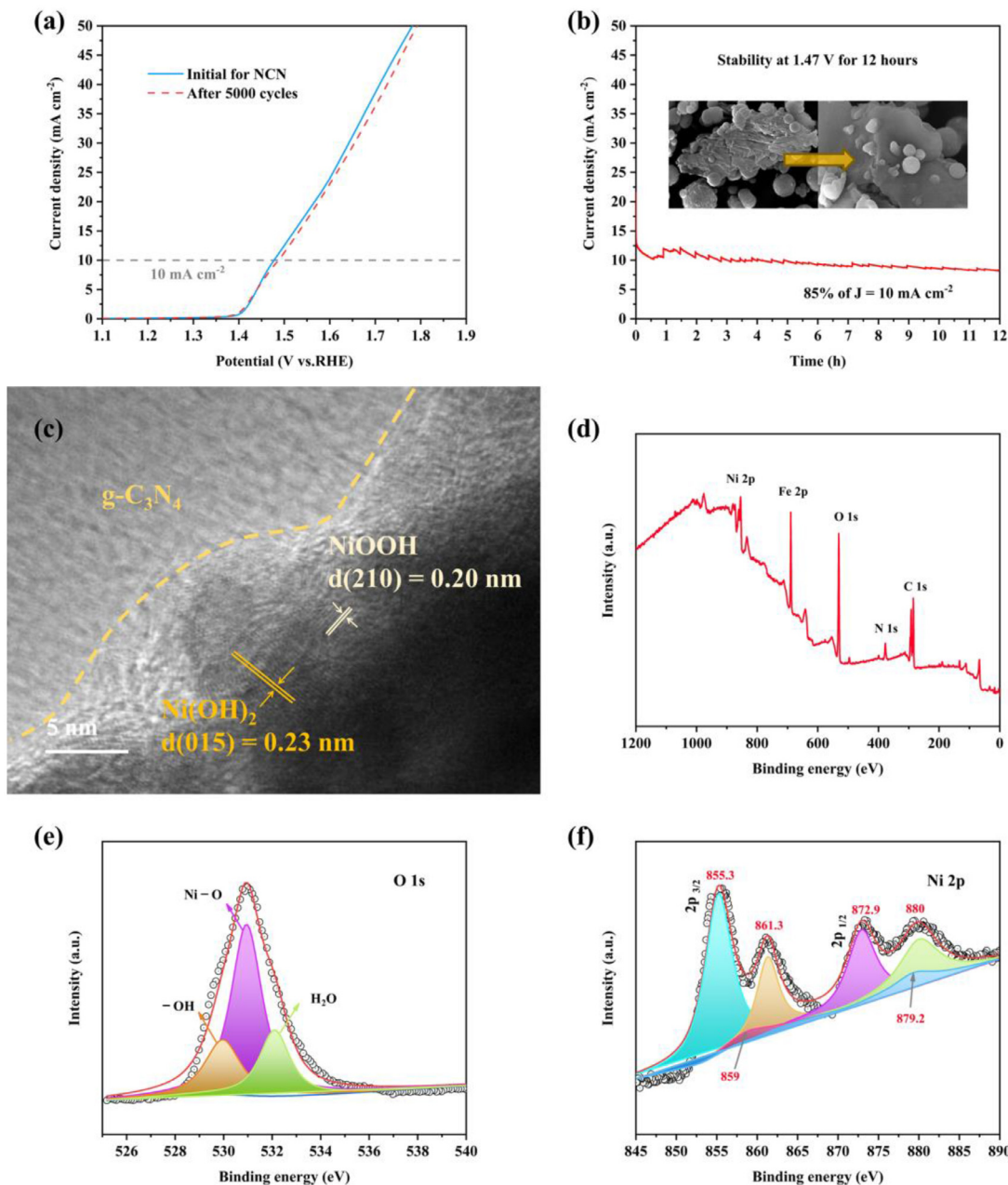


**Fig. 7.** Stability tests of NCN for 5000 cycles of CV (a); chronoamperometry test of NCN composite catalyst at constant potential of 1.47 V (vs. RHE) in 0.1 M KOH solution. Insets are the SEM images of NCN before and after the test (b); HRTEM image (c), XPS spectrum (d), and high-resolution O 1s (e) and Ni 2p (f) XPS spectra of NCN after the long-term test.

cate the formation of NiOOH during long-term OER test, which is considered as the active species towards OER [53]. The XPS survey spectrum (Fig. 7d) show the presence of Fe in NCN after long-term test, which comes from KOH solution. It has been reported that Fe ions promote the transformation of Ni(OH)<sub>2</sub> to NiOOH during OER, and further boost the activity of NiOOH by its electronic structure [54–56]. During the OER test, the Fe elements in KOH could act as

Fe source, which gradually incorporated into NCN, promoting the formation of NiOOH.

The outstanding electrocatalytic activity and durability of NCN can be described to the following points: (1) the addition of LCN affords an abundance of active sites for OH<sup>-</sup> adsorption, due to its satisfied surface areas and stable two-dimensional layered structure; (2) outstanding potential catalytic activity of Ni(OH)<sub>2</sub> and

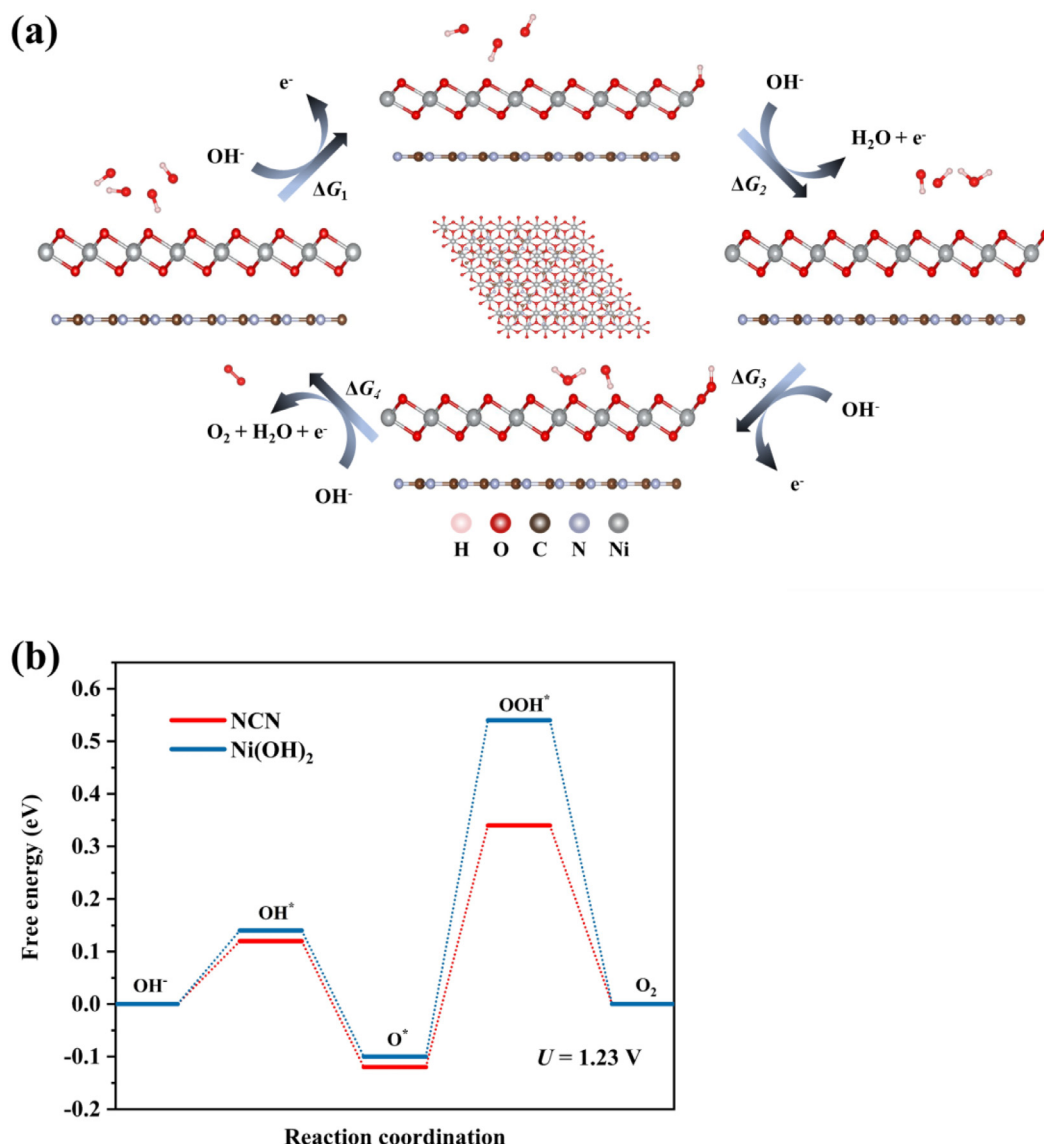
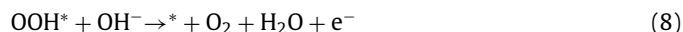
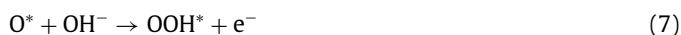


**Fig. 8.** (a) Model and adsorption geometries of NCN for four OER steps: left, substrate and OH<sup>-</sup>; top-middle, adsorbed OH; right, adsorbed O; bottom-middle, adsorbed OOH. Insert image is the top view of the NCN heterojunction. (b) Free-energy landscape of NCN (red) and Ni(OH)<sub>2</sub> (blue) at  $U = 1.23$  V.

high activity of NiOOH, which is transformed from Ni(OH)<sub>2</sub> during OER process; (3) Fe impurities in Ni(OH)<sub>2</sub>/NiOOH from KOH solution could enhance OER performance; (4) coupling of NCN heterojunction. These reasons reveal NCN as a promising non-precious metal based OER catalyst in the field of electrochemistry. However, the role of heterojunction remains unclear at the level of atoms, therefore, additional DFT theoretical calculations were applied.

### 3.5. DFT theoretical calculations

We carried out density functional theory (DFT) theoretical calculations to explore the principle for the outstanding catalytic properties of NCN composite samples. For the details, the adsorption Gibbs free energy ( $\Delta G$ ) of four steps OER process were calculated as following:



Where \* denotes the reaction site. OH\*, O\* and OOH\* denote the intermediate products during the reactions.  $\Delta G_{1-4}$  represent the reaction free energy for every step. The  $\eta$  could be calculated by the following formula:

$$\eta = (\Delta G_1, \Delta G_2, \Delta G_3, \Delta G_4)_{\max} / \text{e}^- - 1.23 \quad (9)$$

Generally, the reaction rate of the OER is determined by the step that possesses the largest  $\Delta G$ . To be precise, the third reaction step of OOH\* formation is the decisive step for OER process. A smaller  $\Delta G_3$  indicates an easier overall OER reaction. As depicted in Fig. 8b, bare Ni(OH)<sub>2</sub> has the larger  $\Delta G_3$  with an overpotential of 0.64 V, while the overpotential of modified Ni(OH)<sub>2</sub> with additional LCN decreases to 0.46 V. These evidences demonstrate from theoretical calculations that the coupling of Ni(OH)<sub>2</sub> and LCN to form heterojunction can weaken the adsorption of OOH\*, lower the reaction energy barrier and improve the OER catalytic performance.

## 4. Conclusions

In summary, we present a feasible, convenient and nontoxic technological route for the rational design of efficient and inexpensive electrocatalysts. LCN is prepared by a two-step high-temperature thermal peeling process and used to support Ni(OH)<sub>2</sub> microspheres to form NCN heterojunction. This peculiar structure greatly facilitates the exposure of active sites in the multilayer nanosheets, at the same time, stimulates the OER catalytic potential of the metal hydroxides, making charge transfer much easier. Thus, satisfactory catalytic activity and stability, as well as exceptional structural integrity are attributed to the formation of NCN heterojunction. This work may offer a simple route for the discovery of new non-precious metal-based electrocatalysts for OER toward inexpensive cost, excellent performance and outstanding durability.

## Declaration of Competing Interest

We declare that we have no financial and person relationships with people or organizations that can inappropriately influence our work, there is no professional or other personal interest of any nature or kind in any product, service and/or company that could be construed as influencing the position presented in, or the review of, the manuscript entitled.

## Credit authorship contribution statement

**Tong Li:** Formal analysis, Writing – original draft, Writing – review & editing, Validation, Investigation. **Xinxia Ma:** Resources, Data curation, Software. **Jiang Wu:** Conceptualization, Methodology, Software, Supervision, Funding acquisition, Project administration. **Fenghong Chu:** Project administration, Supervision. **Lingxia Qiao:** Resources, Data curation, Software. **Yubao Song:** Resources, Data curation, Software. **Maoliang Wu:** Resources, Data curation, Validation, Visualization, Writing – review & editing. **Jia Lin:** Resources, Data curation. **Lin Peng:** Resources, Data curation, Software. **Zhongwei Chen:** Resources, Data curation, Validation.

## Acknowledgments

This work was partially sponsored by National Natural Science Foundation of China (52076126), Natural Science Foundation of Shanghai (18ZR1416200), Key Laboratory of Clean Power Generation and Environmental Protection Technology in Mechanical Industry.

## Supplementary materials

Supplementary material associated with this article can be found, in the online version, at doi:10.1016/j.electacta.2021.139473.

## References

- [1] S. Anantharaj, S.R. Ede, K. Sakthikumar, K. Karthick, S. Mishra, S. Kundu, Recent trends and perspectives in electrochemical water splitting with an emphasis on sulfide, selenide, and phosphide catalysts of Fe, Co, and Ni: a review, *ACS Catal.* 6 (12) (2016) 8069–8097.
- [2] J.S. Kim, B. Kim, H. Kim, K. Kang, Recent progress on multimetal oxide catalysts for the oxygen evolution reaction, *Adv. Energy Mater.* 8 (11) (2018).
- [3] Z. Wu, L.P. Sun, M. Yang, L.H. Huo, H. Zhao, J.-C. Grenier, Facile synthesis and excellent electrochemical performance of reduced graphene oxide–Co<sub>3</sub>O<sub>4</sub> yolk-shell nanocages as a catalyst for oxygen evolution reaction, *J. Mater. Chem. A* 4 (35) (2016) 13534–13542.
- [4] R. Cao, J.-S. Lee, M. Liu, J. Cho, Recent progress in non-precious catalysts for metal-air batteries, *Adv. Energy Mater.* 2 (7) (2012) 816–829.
- [5] H. Dau, C. Limberg, T. Reier, M. Risch, S. Roggan, P. Strasser, The mechanism of water oxidation: from electrolysis via homogeneous to biological catalysis, *ChemCatChem* 2 (7) (2010) 724–761.
- [6] M.S. Faber, S. Jin, Earth-abundant inorganic electrocatalysts and their nanostructures for energy conversion applications, *Energy Environ. Sci.* 7 (11) (2014) 3519–3542.
- [7] A. Singh, L. Spiccia, Water oxidation catalysts based on abundant 1st row transition metals, *Coord. Chem. Rev.* 257 (17–18) (2013) 2607–2622.
- [8] L.F. Wu, X.S. Wang, Y.P. Sun, Y. Liu, J.H. Li, Flawed MoO<sub>3</sub> belts on graphene template transformed from MoO<sub>3</sub> towards hydrogen evolution reaction, *Nanoscale* 7 (2015) 7040–7044.
- [9] X.Q. Ji, X. Ren, S. Hao, F.Y. Xie, F.L. Qu, G. Du, A.M. Asiri, X.P. Sun, Greatly enhancing the alkaline oxygen evolution reaction activity of NiCo<sub>2</sub>O<sub>4</sub> by amorphous borate shell, *Inorg. Chem. Front.* 4 (2017) 1546–1550.
- [10] S.P. Li, G. Zhang, X.M. Tu, J.H. Li, Polycrystalline CoP/CoP<sub>2</sub> structures for efficient full water splitting, *ChemElectroChem* 5 (2018) 701–707.
- [11] J.X. Zhao, X.H. Li, G.W. Cui, X.P. Sun, Highly-active oxygen evolution electrocatalyzed by a Fe-doped NiCr<sub>2</sub>O<sub>4</sub> nanoparticles film, *Chem. Commun.* 54 (2018) 5462–5465.
- [12] Y. Liang, Y. Li, H. Wang, H. Dai, Strongly coupled inorganic/nanocarbon hybrid materials for advanced electrocatalysis, *J. Am. Chem. Soc.* 135 (6) (2013) 2013–2036.
- [13] Y. Lee, J. Suntivich, K.J. May, E.E. Perry, Y. Shao-Horn, Synthesis and activities of rutile IrO<sub>2</sub> and RuO<sub>2</sub> nanoparticles for oxygen evolution in acid and alkaline solutions, *J. Phys. Chem. Lett.* 3 (3) (2012) 399–404.
- [14] C.C. McCrory, S. Jung, J.C. Peters, T.F. Jaramillo, Benchmarking heterogeneous electrocatalysts for the oxygen evolution reaction, *J. Am. Chem. Soc.* 135 (45) (2013) 16977–16987.
- [15] V. Petrykin, K. Macounova, O.A. Shlyakhtin, P. Krtil, Tailoring the selectivity for electrocatalytic oxygen evolution on ruthenium oxides by zinc substitution, *Angew. Chem. Int. Ed. Engl.* 49 (28) (2010) 4813–4815.
- [16] J. Rossmeisl, Z.W. Qu, H. Zhu, G.J. Kroes, J.K. Nørskov, Electrolysis of water on oxide surfaces, *J. Electroanal. Chem.* 607 (1–2) (2007) 83–89.
- [17] L. Trotochaud, J.K. Ranney, K.N. Williams, S.W. Boettcher, Solution-cast metal oxide thin film electrocatalysts for oxygen evolution, *J. Am. Chem. Soc.* 134 (41) (2012) 17253–17261.
- [18] L.H. Zhuang, L. Ge, Y.S. Yang, M.R. Li, Y. Jia, X.D. Yao, Z.H. Zhu, Ultrathin iron cobalt oxide nanosheets with abundant oxygen vacancies for the oxygen evolution reaction, *Adv. Mater.* 29 (2017) 1606793 201606793.
- [19] C. Tang, N.Y. Cheng, Z.H. Pu, W. Xing, X.P. Sun, NiSe nanowire film supported on nickel foam: an efficient and stable 3D bifunctional electrode for full water splitting, *Angew. Chem. Int. Ed.* 54 (2015) 9351–9355.
- [20] M. Tahir, L. Pan, F. Idrees, X.W. Zhang, L. Wang, J.J. Zou, Z.L. Wang, Electrocatalytic oxygen evolution reaction for energy conversion and storage: a comprehensive review, *Nano Energy* 37 (2017) 136–157.
- [21] D.F. Yan, Y.X. Li, J. Huo, R. Chen, L.M. Dai, S.Y. Wang, Defect chemistry of non-precious-metal electrocatalysts for oxygen reactions, *Adv. Mater.* 29 (2017) 1606459.
- [22] S. Yoon, J.Y. Yun, J.H. Lim, B.Y. Yoo, Enhanced electrocatalytic properties of electrodeposited amorphous cobalt-nickel hydroxide nanosheets on nickel foam by the formation of nickel nanocages for the oxygen evolution reaction, *J. Alloy. Compd.* 693 (2017) 964–969.
- [23] S. Anantharaj, P.E. Karthik, S. Kundu, Petal-like hierarchical array of ultrathin Ni(OH)<sub>2</sub> nanosheets decorated with Ni(OH)<sub>2</sub> nanoburles: a highly efficient OER electrocatalyst, *Catal. Sci. Technol.* 7 (4) (2017) 882–893.
- [24] M. Gao, W. Sheng, Z. Zhuang, Q. Fang, S. Gu, J. Jiang, Y. Yan, Efficient water oxidation using nanostructured alpha-nickel-hydroxide as an electrocatalyst, *J. Am. Chem. Soc.* 136 (19) (2014) 7077–7084.
- [25] X. Hu, G. Luo, X. Guo, Q. Zhao, R. Wang, G. Huang, B. Jiang, C. Xu, F. Pan, Origin of the electrocatalytic oxygen evolution activity of nickel phosphides: in-situ electrochemical oxidation and Cr doping to achieve high performance, *Sci. Bull.* 66 (7) (2021) 708–719.
- [26] C. Manjunatha, N. Srinivasa, S.K. Chaitra, M. Sudeep, R.Chandra Kumar, S. Ashoka, Controlled synthesis of nickel sulfide polymorphs: studies on the effect of morphology and crystal structure on OER performance, *Mater. Today Energy* 16 (2020).
- [27] A.K. Tareen, G.S. Priyanga, K. Khan, E. Pervaiz, T. Thomas, M. Yang, Nickel-Based Transition Metal Nitride Electrocatalysts for the Oxygen Evolution Reaction, *ChemSusChem* 12 (17) (2019) 3941–3954.
- [28] S. Anantharaj, P.E. Karthik, S. Kundu, Petal-like hierarchical array of ultrathin Ni(OH)<sub>2</sub> nanosheets decorated with Ni(OH)<sub>2</sub> nanoburles: a highly efficient OER electrocatalyst, *Catal. Sci. Technol.* 7 (4) (2017) 882–893.
- [29] X.J. Zhang, L. Tao, P. He, X.Q. Zhang, M.Q. He, F.Q. Dong, S.Y. He, C.X. Li, H.H. Liu, S. Wang, Y. Zhang, A novel cobalt hexacyanoferrate/multi-walled carbon nanotubes nanocomposite: spontaneous assembly synthesis and application as electrode materials with significantly improved capacitance for supercapacitors, *Electrochim. Acta* 259 (2018) 793–802.
- [30] J. Yu, Q.Q. Li, C.Y. Xu, N. Chen, Y. Li, H.G. Liu, L. Zhen, V.P. Dravid, J.S. Wu, NiSe<sub>2</sub> pyramids deposited on N-doped graphene encapsulated Ni foam for high-performance water oxidation, *J. Mater. Chem. A* 5 (2017) 3981–3986.
- [31] S. Xu, P. Zhou, Z. Zhang, C. Yang, B. Zhang, K. Deng, S. Bottle, H. Zhu, Selective oxidation of 5-hydroxymethylfurfural to 2,5-furandicarboxylic acid using O<sub>2</sub> and a photocatalyst of co-thiophenopyrazine bonded to g-C<sub>3</sub>N<sub>4</sub>, *J. Am. Chem. Soc.* 139 (41) (2017) 14775–14782.
- [32] J. Yi, W. El-Alami, Y. Song, H. Li, P.M. Ajayan, H. Xu, Emerging surface strategies on graphitic carbon nitride for solar driven water splitting, *Chem. Eng. J.* 382 (2020).
- [33] Y. Zheng, Y. Jiao, Y.H. Zhu, Q.R. Cai, A. Vasileff, L.H. Li, Y. Han, Y. Chen, S.Z. Qiao, Molecule-level g-C<sub>3</sub>N<sub>4</sub> coordinated transition metals as a new class



- of electrocatalysts for oxygen electrode reactions, *J. Am. Chem. Soc.* 139 (2017) 3336–3339.
- [34] S. Gahlot, F. Dappozze, S. Mishra, C. Guillard, High surface area g-C<sub>3</sub>N<sub>4</sub> and g-C<sub>3</sub>N<sub>4</sub>-TiO<sub>2</sub> photocatalytic activity under UV and visible light: impact of individual component, *J. Environ. Chem. Eng.* 9 (4) (2021).
- [35] H.T. Ren, S.Y. Jia, Y. Wu, S.H. Wu, T.H. Zhang, X. Han, Improved photochemical reactivities of Ag<sub>2</sub>O/g-C<sub>3</sub>N<sub>4</sub> in phenol degradation under UV and visible light, *Ind. Eng. Chem. Res.* 53 (45) (2014) 17645–17653.
- [36] X. Li, G.Q. Han, Y.R. Liu, B. Dong, X. Shang, W.H. Hu, Y.M. Chai, Y.Q. Liu, C.G. Liu, In situ grown pyramid structures of nickel diselenides dependent on oxidized nickel foam as efficient electrocatalyst for oxygen evolution reaction, *Electrochim. Acta* 205 (2016) 77–84.
- [37] Y. Qin, H. Li, H. Dong, C. Ma, X. Li, X. Liu, Y. Liu, C. Li, Y. Yan, Enhanced photocatalytic performance and stability of visible-light-driven Z-scheme CdS/Ag/g-C<sub>3</sub>N<sub>4</sub> nanosheets photocatalyst, *New J. Chem.* 42 (15) (2018) 12437–12448.
- [38] W.X. Zou, B. Deng, X.X. Hu, Y.P. Zhou, Y. Pu, S.H. Yu, K.L. Ma, J.F. Sun, H.Q. Wan, L. Dong, Crystal-plane-dependent metal oxide-support interaction in CeO<sub>2</sub>/g-C<sub>3</sub>N<sub>4</sub> for photocatalytic hydrogen evolution, *Appl. Catal. B Environ.* 238 (2018) 111–118.
- [39] L.X. Wang, Y. Li, X.C. Yin, Y.Z. Wang, A.L. Song, Z.P. Ma, X.J. Qin, G.J. Shao, Coral-like structured Ni/C<sub>3</sub>N<sub>4</sub> composite coating: an original catalyst for hydrogen evolution reaction in alkaline solution, *ACS Sustain. Chem. Eng.* 5 (2017) 7993–8003.
- [40] Y.J. Zhong, Z.Q. Wang, J.Y. Feng, S.C. Yan, H.T. Zhang, Z.S. Li, Z.G. Zou, Improvement in photocatalytic H<sub>2</sub> evolution over g-C<sub>3</sub>N<sub>4</sub> prepared from protonated melamine, *Appl. Surf. Sci.* 295 (2014) 253–259.
- [41] S. Wang, P. He, L. Jia, M. He, T. Zhang, F. Dong, M. Liu, H. Liu, Y. Zhang, C. Li, J. Gao, L. Bian, Nanocoral-like composite of nickel selenide nanoparticles anchored on two-dimensional multi-layered graphitic carbon nitride: a highly efficient electrocatalyst for oxygen evolution reaction, *Appl. Catal. B* 243 (2019) 463–469.
- [42] C. Kong, F. Zhang, X. Sun, C. Kai, W. Cai, In-situ grown rod-shaped Ni(OH)<sub>2</sub> between interlayer of g-C<sub>3</sub>N<sub>4</sub> for hydrogen evolution under visible light, *Inorg. Chem. Commun.* 122 (2020).
- [43] J. Zheng, R. Zhang, X. Wang, P. Yu, Hydrothermally synthesized Ni(OH)<sub>2</sub>@Zn(OH)<sub>2</sub> composite with enhanced electrochemical performance for supercapacitors, *Res. Chem. Intermed.* 44 (2018) 6637–6648.
- [44] J. Oh, R.J. Yoo, S.Y. Kim, Y.J. Lee, D.W. Kim, S. Park, Oxidized carbon nitrides: water-dispersible, atomically thin carbon nitride-based nanodots and their performances as bioimaging probes, *Chem. Eur. J.* 21 (2015) 6241–6246.
- [45] J.H. Kim, D.H. Youn, K. Kawashima, J. Lin, H. Lim, C.B. Mullins, An active nanoporous Ni(Fe) OER electrocatalyst via selective dissolution of Cd in alkaline media, *Appl. Catal. B Environ.* 225 (2018) 1–7.
- [46] S.L. Zhao, Y. Wang, J.C. Dong, C.T. He, H.J. Yin, P.F. An, K. Zhao, X.F. Zhang, C. Gao, L.J. Zhang, J.W. Lv, J.X. Wang, J.Q. Zhang, A.M. Khattak, N.A. Khan, Z.X. Wei, J. Zhang, S.Q. Liu, H.J. Zhao, Z.Y. Tang, Ultrathin metal-organic framework nanosheets for electrocatalytic oxygen evolution, *Nat. Energy* 1 (2016) 1–10.
- [47] H. Wang, A. Xie, X. Li, Q. Wang, W. Zhang, Z. Zhu, J. Wei, D. Chen, Y. Peng, S. Luo, Three-dimensional petal-like graphene Co<sub>3.0</sub>Cu<sub>1.0</sub> metal organic framework for oxygen evolution reaction, *J. Alloy. Compd.* 884 (2021).
- [48] H. Wang, Y. Yang, Y. Ren, D. Chen, J. Wei, L. Wang, A. Xie, S. Luo, Electrochemical synthesis of Pt nanoparticles on ZrO<sub>2</sub>/MWCNTs hybrid with high electrocatalytic performance for methanol oxidation, *J. Electroanal. Chem.* 898 (2021).
- [49] A. Xie, H. Wang, Z. Zhu, W. Zhang, X. Li, Q. Wang, S. Luo, Mesoporous CeO<sub>2</sub>-α-MnO<sub>2</sub>-reduced graphene oxide composite with ultra-high stability as a novel electrode material for supercapacitor, *Surf. Interfaces* 25 (2021).
- [50] A. Xie, J. Du, F. Tao, Y. Tao, Z. Xiong, S. Luo, X. Li, C. Yao, Three-dimensional graphene surface-mounted nickel-based metal organic framework for oxygen evolution reaction, *Electrochim. Acta* 305 (2019) 338–348.
- [51] Z. Liu, B. Tang, X. Gu, H. Liu, L. Feng, Selective structure transformation for NiFe/NiFe<sub>2</sub>O<sub>4</sub> embedded porous nitrogen-doped carbon nanosphere with improved oxygen evolution reaction activity, *Chem. Eng. J.* 395 (2020).
- [52] K. Wan, J. Luo, X. Zhang, P. Subramanian, J. Fransaer, In-situ formation of Ni (oxy)hydroxide on Ni foam as an efficient electrocatalyst for oxygen evolution reaction, *Int. J. Hydrog. Energy* 45 (15) (2020) 8490–8496.
- [53] Y.F. Li, A. Selloni, Mechanism and activity of water oxidation on selected surfaces of pure and Fe-doped NiO<sub>x</sub>, *ACS Catal.* 4 (4) (2014) 1148–1153.
- [54] D. Friebe, M.W. Louie, M. Bajdich, K.E. Sanwald, Y. Cai, A.M. Wise, M.J. Cheng, D. Sokaras, T.C. Weng, R. Alonso-Mori, R.C. Davis, J.R. Bargar, J.K. Nørskov, A. Nilsson, A.T. Bell, Identification of highly active Fe sites in (Ni,Fe)OOH for electrocatalytic water splitting, *J. Am. Chem. Soc.* 137 (3) (2015) 1305–1313.
- [55] S. Klaus, Y. Cai, M.W. Louie, L. Trotochaud, A.T. Bell, Effects of Fe electrolyte impurities on Ni(OH)<sub>2</sub>/NiOOH structure and oxygen evolution activity, *J. Phys. Chem. C* 119 (13) (2015) 7243–7254.
- [56] L. Trotochaud, S.L. Young, J.K. Ranney, S.W. Boettcher, Nickel-iron oxyhydroxide oxygen-evolution electrocatalysts: the role of intentional and incidental iron incorporation, *J. Am. Chem. Soc.* 136 (18) (2014) 6744–6753.